Self-Adapting Graphitic C_6N_6-Based Copper Single-Atom Catalyst for Smart Biosensors

Qing Hong, Hong Yang, Yanfeng Fang, Wang Li, Caixia Zhu, Zhuang Wang, Sicheng Liang, Xuwen Cao, Zhixin Zhou, Yanfei Shen, Songqin Liu, Yuanjian Zhang*

Jiangsu Engineering Laboratory of Smart Carbon-Rich Materials and Device, Jiangsu Province Hi-Tech Key Laboratory for Bio-Medical Research, State Key Laboratory of Bioelectronics, School of Chemistry and Chemical Engineering, Medical School, Southeast University, Nanjing 211189, China, Email: Yuanjian.Zhang@seu.edu.cn

Abstract

Self-adaptability is highly envisioned for artificial devices such as robots with chemical noses. For this goal, seeking catalysts with multiple and modulable reaction pathways is promising but generally hampered by inconsistent reaction conditions. Herein, we report a self-adaptive $Cu_{SA}C_6N_6$ single-atom catalyst having two reactive oxygen-oriented pathways under the same reaction conditions. $Cu_{SA}C_6N_6$ consisted of coordinated peroxidase-like Cu-N coordination centers and photo-responsive donor-π-acceptor (D-π-A) units with promoted intramolecular charge separation and migration. Interestingly, it drove the basic oxidation of peroxidase substrates by the bound copper-oxo pathway, and undertook a second gain reaction triggered by light via the free hydroxyl radical pathway under the same conditions. A remarkable basic activity and a superb gain of up to 3.6 times under household lights were observed, significantly higher than that of its control systems, including solo carbon nitride-based nanozymes or photocatalysts, their mixtures, and even that under thermal stimuli to the maximum endured temperature for most lives. As an application, the self-adapting $Cu_{SA}C_6N_6$ was used to construct a glucose biosensor, which can intelligently switch the linear detection range and sensitivity to a diverse range of concentrations in vitro.

Keywords: carbon nitride, single-atom catalysts, donor-π-acceptor, self-adaptability, smart biosensors

Introduction

Establishment of indispensable adaptability plays a crucial role in living systems under a wide variety of environmental stimuli. For example, under normal conditions, thyroid hormones are primarily responsible for the regulation of metabolism at the basal level in humans. Nonetheless, when suddenly exposed to severe cold stimuli, the sympathetic nervous system releases high concentrations of norepinephrine. It significantly accelerates metabolism as the second pathway, which produces more heat to compensate for the cold. It features a primary transduction in the normal state and a large gain in exceptional circumstances. For the same reason, mimicking such self-adaptability is highly envisioned in artificial devices,[1-3] such as robots, brain-machine interfaces, and the Internet of Things, to freely perceive weak and strong external signals, but remains a grand challenge. From a chemical point of view, to realize these imperative basic activity and prominent gain effect, seeking catalysts with multiple and modulable reaction pathways is the crux of the matter.[4-9] However, the inconsistency of reaction conditions, such as temperature, pH, and solvents, generally exists in different reaction pathways, hampering the effective coordinating of multiple catalytic pathways simultaneously.[10]

As a metal-free semiconductor, polymeric carbon nitride (PCN) has been intensively explored not only as a metal-free photocatalyst[11-20] but also as a solid ligand to anchor single metal atom,[21-23] owing to its engineerable conjugated repetitive units, rich lone pair electrons in the framework, and high physicochemical stability. For example, carbon nitrides with different topological structures (e.g., C_3N_4, C_3N_2, C_5N_2, and C_2N) [24-30]and metal dopants (e.g., K and Cu)[31-33] have been developed for a wide range of photocatalytic oxidation reactions[34-37] (e.g., clean water and sanitation) and oxidase[38-41]/peroxidase-like[42-44] activities. Interestingly, these oxidation reactions are catalyzed by carbon nitrides via different reactive oxygen-related intermediates under similar conditions, except for light irradiation.[45-49] As such, we reason that the multiformity of carbon nitrides in oxidation processes would offer an intriguing way to solve the

inconsistency of reaction conditions in realizing the basic activity and the gain effect for self-adaptability; however, to our knowledge, this has rarely been reported.

Herein, we report a copper single-atom catalyst based on highly conjugated carbon nitride ($Cu_{SA}C_6N_6$) to mimic self-adaptability from nature. $Cu_{SA}C_6N_6$ could not only drive a basic oxidation of peroxidase substrates through bound high-valent copper-oxo pathway, but also initiate a second gain reaction under light irradiation via free hydroxyl radical pathway under the same conditions. As a result, $Cu_{SA}C_6N_6$ demonstrated a conspicuous basic activity and a superb gain up to 3.6 times under household light. It was significantly higher than that of its control systems, including solo carbon nitride-based peroxidase-like catalysts or photocatalysts, their mixtures, and even that under thermal stimuli to the maximum endured temperature for most lives. In a proof-of-concept application, under light of different intensity, $Cu_{SA}C_6N_6$ was successfully applied to a single glucose sensor with intelligent switching of linear detection range and sensitivity to a diverse range of concentrations in vitro.

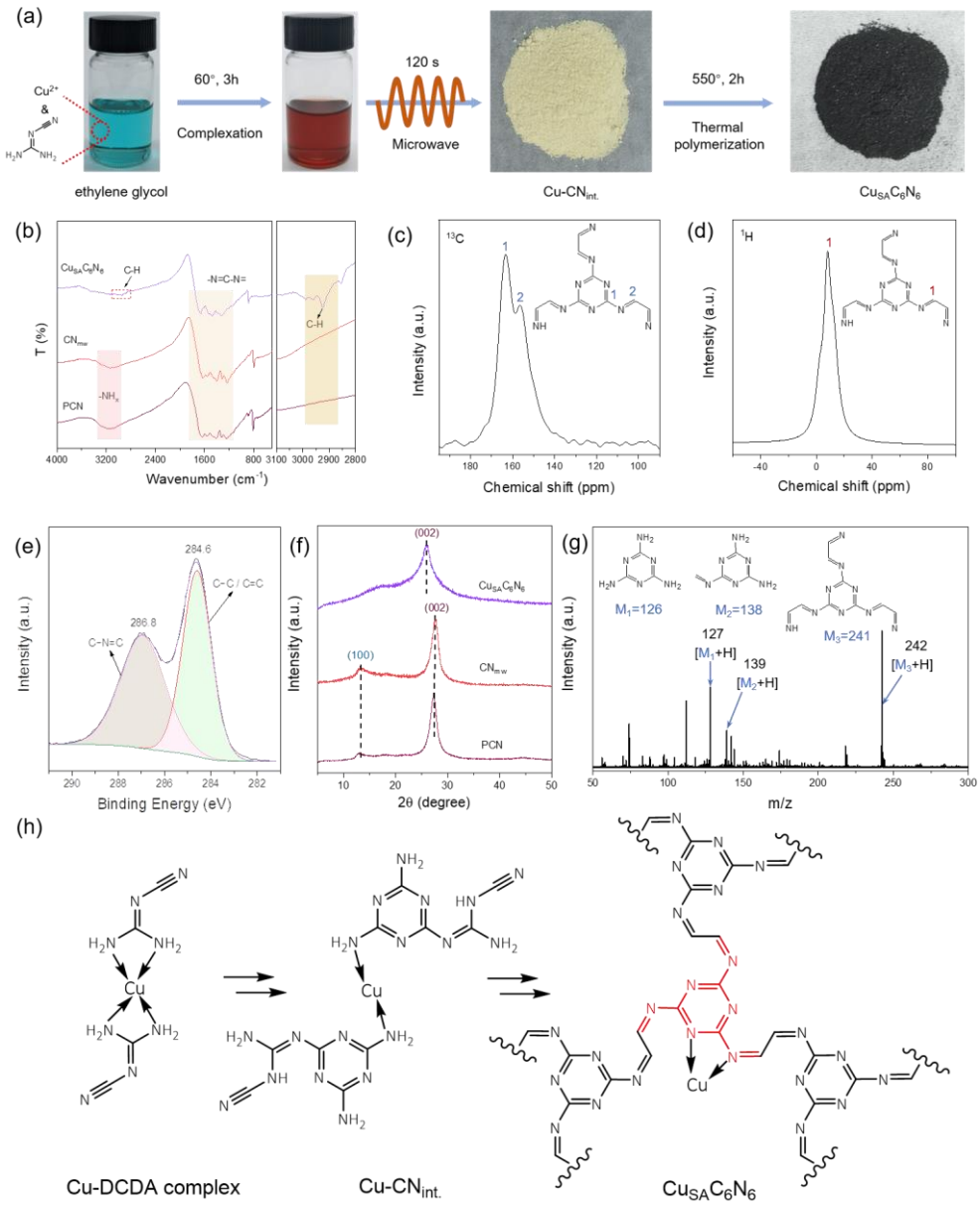

Fig. 1 Preparation and molecular structure of $Cu_{SA}C_6N_6$. (a) Brief Synthesis procedure for $Cu_{SA}C_6N_6$. (b) FT-IR spectra of $Cu_{SA}C_6N_6$, CN_{mw} and PCN. Solid-state (c) ^{13}C and (d) ^{1}H NMR spectra of $Cu_{SA}C_6N_6$. (e) C 1s XPS spectrum of $Cu_{SA}C_6N_6$. (f) Normalized XRD patterns of $Cu_{SA}C_6N_6$, CN_{mw}, and PCN. (g) LDI-TOF mass spectrum of $Cu_{SA}C_6N_6$. (h) Proposed condensation processes and molecular structure of $Cu_{SA}C_6N_6$.

Results and Discussion

Synthesis and molecular structure of $Cu_{SA}C_6N_6$

As illustrated in **Fig. 1a**, copper acetate, as the Cu source, was first complexed with

dicyandiamide (DCDA) in ethylene glycol (EG) at 60 °C for 3 h to produce a reddish-brown DCDA-Cu complex. Subsequently, microwave-assisted condensation[36] using EG as the solvent was utilized to synthesize the pale-yellow intermediate, denoted as Cu-$CN_{int.}$, with a yield of 85%. Owing to the pre-coordinated Cu-DCDA complex in EG, the possible formation of a metal or metallic oxide in Cu-$CN_{int.}$ was avoided. As displayed in **Fig. S1**, the X-ray diffraction (XRD) pattern of Cu-$CN_{int.}$ showed the only peak at 26.7°, assigning to an interlayer stacking. In contrast, the microwave-assisted polymerization of the blue Cu^{2+} and DCDA mixture resulted in a product with additional XRD peaks for CuO, indicating the significance of pre-complexation in the preservation of the single-atom state. The final product, $Cu_{SA}C_6N_6$, was obtained via thermal polymerization at 550 °C. As a control, CN_{mw} was fabricated by the same microwave-assisted polymerization of DCDA in EG without copper and subsequent thermal condensation.

The combustion elemental analysis in **Table S1** shows the transformation of the molar C/N value from Cu-$CN_{int.}$ of 0.73 to $Cu_{SA}C_6N_6$ of 0.95, which is approximately 1. FTIR spectroscopy was used to determine the chemical structure of the new carbon nitride (**Fig. 1b**). The FTIR spectrum of $Cu_{SA}C_6N_6$ showed strong vibration peaks around 800 and 1200-1700 cm^{-1}, assigning to typical triazine rings (CN heterocycles). A characteristic peak at approximately 2900 cm^{-1}, which was ascribed to C–H stretching,[50] was also observed. Solid-state NMR spectroscopy provided further insights into the nature of the building blocks of $Cu_{SA}C_6N_6$. As shown in **Fig. 1c**, the carbon atoms in the triazine units corresponded to the peak at approximately 163 (1) ppm, confirming the existence of conjugated triazine rings in $Cu_{SA}C_6N_6$. The adjacent chemical shift at *ca.* 156 (2) ppm was assigned to the carbon atom indirectly connected to the triazine ring.[51] Those two types of carbon atoms and FTIR spectrum demonstrated the existence of triazine rings and non-cyclization groups of -N=CH-. The ^1H magic angle spinning (MAS) NMR spectrum was also employed to determine the local environment of the H atom. As shown in **Fig. 1d**, the ^1H NMR spectrum of $Cu_{SA}C_6N_6$ exhibited a main characteristic peak around 8.3 ppm, ascribing to the -

N=CH- group. Notably, this chemical shift of the ^{1}H NMR spectrum was often assigned to the aromatic carbon environment,[52] indicating the existence of a triazine ring and a second conjugated carbon atom.

The high-resolution X-ray photoelectron spectroscopy (XPS) in **Fig. 1e** provided additional bonding information. The C1s XPS spectra exhibited two main peaks at 284.6 eV (C1) and 286.8 eV (C2), which were attributed to C-C peak and C species in triazine rings (C−N=C), respectively.[53] Interestingly, the carbon peak (ca. 284.6 eV) in PCN and CN_{mw} was assigned to random adventitious carbon, while C-$(N)_3$ shifted to a high binding energy at 288.1 eV (**Fig. S2**). These results demonstrated that the non-cyclization group of -N=CH- was coupled, forming -N=CH-CH=N- moieties in the thermal polymerization process. The crystalline texture was further explored using XRD spectroscopy (**Fig. 1f**). Compared to PCN and CN_{mw}, the diffraction peak of $Cu_{SA}C_6N_6$ at *ca.* 26.0° (002) corresponding to interlayer stacking reflection (002), was broadened and down-shifted, indicating a slightly enlarged interlayer spacing which may arise from the insertion of Cu atoms between C_6N_6 layers.

To verify the precise molecular structure of $Cu_{SA}C_6N_6$, matrix-free laser desorption/ionization time-of-flight (LDI-TOF) mass spectra were measured. The m/z peaks resulted from the ablation products of the repetitive C_6N_6 units in $Cu_{SA}C_6N_6$. **Fig. 1g** illustrates a series of m/z peaks, including $[M + H^+]$ of 127.11, assigning to $C_3N_6H_6$ (M_1, melamine, calc.: 126), m/z $[M + H^+]$ of 139.15 attributable to $C_4N_6H_6$ (M_2, calc.: 138), and m/z $[M + H^+]$ of 242.15 attributable to $C_9N_9H_7$ (M_3, calc.: 241). The other m/z peaks shown in **Fig. S3**, also supported the ablation unit's information. Therefore, these structural explorations demonstrated that $Cu_{SA}C_6N_6$ featured a repetitive basic triazine core and a -N=CH-CH=N- linker. The possible condensation processes and the molecular structure of $Cu_{SA}C_6N_6$ are shown in **Fig. 1h**.

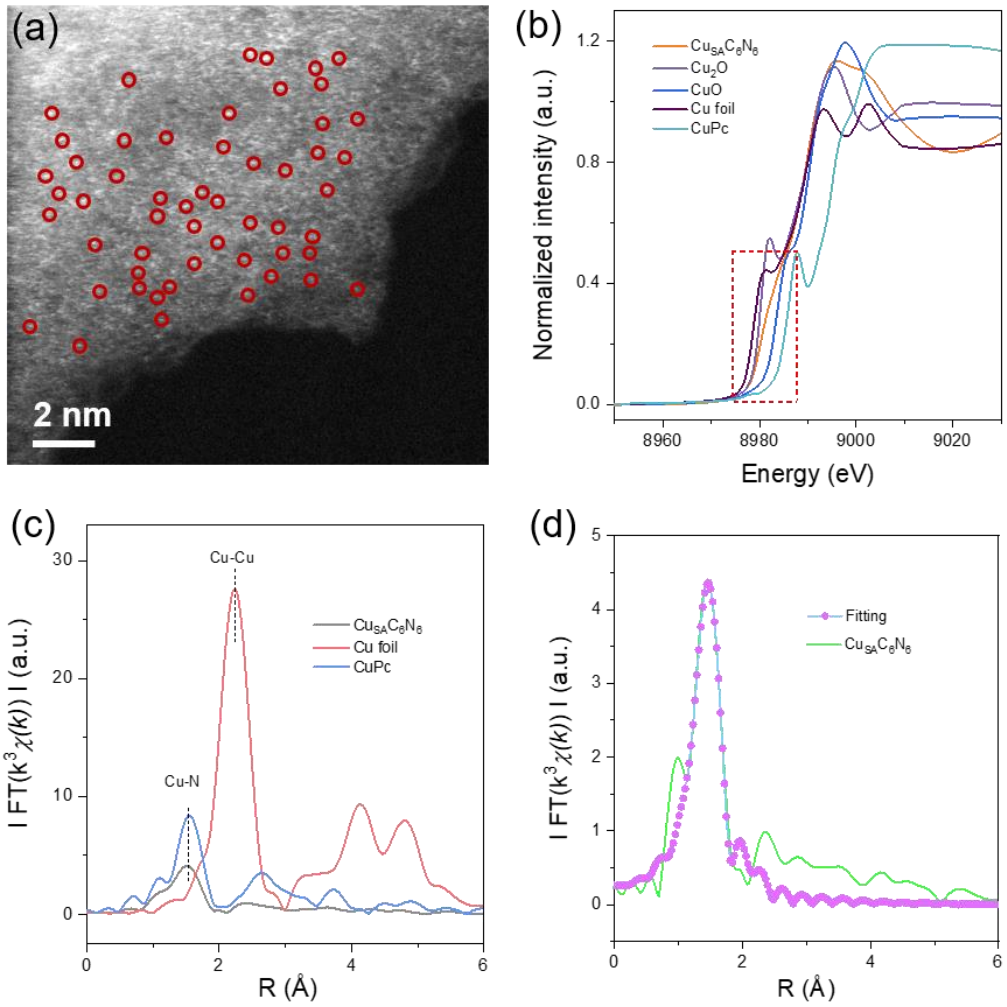

Fig. 2 Morphologies and synchrotron XAFS measurements of $Cu_{SA}C_6N_6$. (a) HAADF-TEM image of $Cu_{SA}C_6N_6$. (b) Cu k-edge XANES profiles of Cu foil, Cu_2O, CuO, $Cu_{SA}C_6N_6$, and CuPc. (c) Cu k-edge EXAFS spectra in R-space of the $Cu_{SA}C_6N_6$, CuPc, and Cu foil samples. (d) EXAFS fitting curve for $Cu_{SA}C_6N_6$ in R-space.

Cu single-atom structure of $Cu_{SA}C_6N_6$

The scanning electron microscopy (SEM) images in **Fig. S4a** shows the disordered and porous structure of $Cu_{SA}C_6N_6$, which distinguishes it from the blocky structures of PCN and CN_{mw} **(Fig. S4b and c)**. The high-resolution TEM images in **Fig. S5** revealed the ultrathin nanosheet-like morphology of $Cu_{SA}C_6N_6$ and no obvious Cu/CuO nanoparticles existed on the surface of C_6N_6 framework, which were in agreement with the XRD results. The large-area high-angle annular dark-field scanning transmission electron microscopy (HAADF-STEM) image (**Fig. 2a**) corroborated the existence of

uniformly dispersed single-atom Cu on the C_6N_6 matrix, evident by abundant isolated bright spots highlighted by a red circle. The high Cu content in $Cu_{SA}C_6N_6$ was quantitatively measured by inductively coupled plasma mass spectrometry (ICP-MS) as ~2.36 wt %. The corresponding STEM-EDS elemental mapping images show that the C, N, and Cu species were atomically and homogeneously dispersed across the entire C_6N_6 nanosheet (**Fig. S6**).

To further investigate chemical state and local coordination environment of Cu species in $Cu_{SA}C_6N_6$, X-ray absorption fine structure (XAFS) measurements of the Cu K-edge were performed. From the normalized Cu K-edge X-ray absorption near-edge structure (XANES) spectra (**Fig. 2b**), the absorption edge of $Cu_{SA}C_6N_6$ was located between the control samples of Cu foil and CuO, indicating that the coexisting Cu^+ (which acted as a predominant oxidation state)[54] and Cu^{2+} carried a partial positive charge between 0 and +2. Meanwhile, the related FT k^3-weighted Extended X-ray absorption fine structure (EXAFS) spectrum in the R space for $Cu_{SA}C_6N_6$ was also measured (**Fig. 2c**). The presence of a characteristic peak located at 1.51 Å indicated the first coordination shell of Cu-N. Furthermore, there was no obvious metallic Cu-Cu interaction at around 2.2 Å, demonstrating that Cu atoms were atomically dispersed in the $Cu_{SA}C_6N_6$ matrix. This result was consistent with the HAADF-STEM images. To further explore the atomic coordination of Cu, the related FT k^3-weighted EXAFS fitting in R-spaces (**Fig. 2d**) was performed to reveal the detailed structural information.[55] The fitting analysis result (**Table S2**) showed that the average Cu-N coordination number in the first coordination shell was 2.0 and the Cu-N bond length was 1.93 Å, indicating that one Cu atom was coordinated by two N atoms, forming a $Cu\text{-}N_2$ moiety.

The existence of Cu-N chemical bonding information was also verified by the N 1s and Cu 2p XPS spectra. As shown in **Fig. S7**, the N 1s peak could be deconvoluted into four peaks, in which the dominant N species around 398.0 eV was mainly ascribed to the formation of pyridinic nitrogen (C═N-C) in triazine rings; The peak at 399.7 eV and 400.7 eV were corresponding to pyrrolic N and graphitic N. Interestingly, a new bond at 398.7 eV was observed, demonstrating the formation of a Cu-N bond, which was

also in agreement with the EXAFS spectrum in the R space measurements (**Fig. 2c**). The Cu 2p spectrum (**Fig. S8**) exhibited two main peaks with binding energy of 932.9 and 952.9 eV, which were assigned to Cu $2p^{3/2}$ and Cu $2p^{1/2}$, respectively. Furthermore, a weak satellite peak was recorded at 944.8 eV, indicating the presence of Cu^{2+} species in $Cu_{SA}C_6N_6$. The spectrum for Cu $2p^{3/2}$ could be deconvoluted into two peaks at 932.6 and 934.8 eV, corresponding to Cu^{1+} and Cu^{2+}, respectively.[56, 57] This result further proved the coexistence of Cu^{+} and Cu^{2+} in $Cu_{SA}C_6N_6$, consisting with the XANES spectroscopy (**Fig. 2b**).

Basic catalytic activity and Gain effect of $Cu_{SA}C_6N_6$

The filling of Cu-N coordination into C_6N_6 framework endowed it with basic peroxidase-like catalytic activity. As shown in **Fig. 3a** and **S9**, taking catalytic oxidation of 2, 2'-azino-bis (3-ethylbenzothiazoline-6-sulfonic acid) (ABTS) in the presence of H_2O_2 as the model reaction, an evident color change from transparency to green was observed.[58] Moreover, owing to the π-conjugated hybridization of energy levels along the polymer linker and π-stacking between linkers, $Cu_{SA}C_6N_6$ demonstrated a narrow optical gap (1.30 eV, **Fig. S10, S11**). Thus, $Cu_{SA}C_6N_6$ was able to effectively utilize the lower excitation energy of light to realize a gain. As shown in **Fig. 3c**, when irradiated by a household white LED lamp (400-900 nm, 50 mW/cm^2, **Fig. S12**), the color of $ABTS_{ox}$ turned dark green, indicating considerable enhancement in the oxidation of ABTS. The quantitative absorbance of $ABTS_{ox}$ at 417 nm under light irradiation (0.72) was 3.6 times than that in the dark (0.20). This result was equivalent to an improved total peroxidase-like rate constant of 3.4 times (**Fig. S13**).

In contrast to $Cu_{SA}C_6N_6$, the basic catalytic activities of control PCN and CN_{mw} were negligible (**Fig. 3b**). Under light irradiation, their catalytic activities were enhanced, indicative of typical photocatalysts, but were still much lower than that of $Cu_{SA}C_6N_6$. This result demonstrated that the basic activity of photocatalysts without external light irradiation is essentially lacking, which is indispensable for maintaining imperative activity in normal mode. To further understand the excellent basic activity and gain

effect of $Cu_{SA}C_6N_6$, two well-known copper-containing nanozymes, i.e., Cu^{2+}-PCN and Cu-N-C with similar Cu-N coordination were also prepared. Interestingly, although higher basic activities of Cu^{2+}-PCN and Cu-N-C were observed (**Fig. 3b**), none of them demonstrated a similar large gain effect as $Cu_{SA}C_6N_6$ under light irradiation, indicating that the second reaction pathway was not effectively initiated. For the former, although charge separation would occur in the C_3N_4 framework under light irradiation, the Cu ions significantly quenched it as recombination sites. For the latter, the graphitic carbon framework has intrinsically poor charge-separation ability. These results indicated that most conventional catalysts were only applicable for effectively driving a single enzyme-like or photocatalytic reaction because of the inconsistency in the requirements for basic and gain reactions. It was supposed that the unique conjugated linkers (-N=CH-CH=N-) not only elongated the distance of D-A to reduce recombination at Cu sites but also simultaneously compensated for the charge transfer between D-A in $Cu_{SA}C_6N_6$, leading to synergistic two-pathway catalytic reactions.

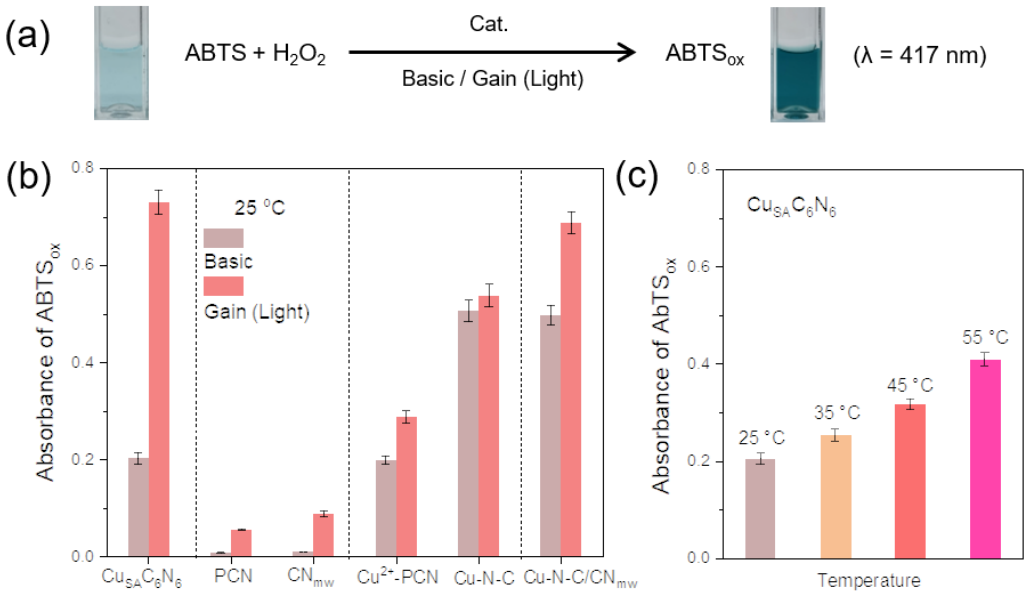

Fig. 3 Gain effect evaluation by the standard ABTS catalytic oxidation. (a) Equation and photographs of standard ABTS catalytic oxidation using different catalysts as shown in (b) and (c). (b) Absorbance of $ABTS_{ox}$ catalyzed by $Cu_{SA}C_6N_6$, PCN, CN_{mw}, Cu^{2+}-PCN, Cu-N-C and Cu-N-C/CN_{mw} without (basic) and with (gain) light irradiation. (c) Absorbance of $ABTS_{ox}$ catalyzed by $Cu_{SA}C_6N_6$ at different temperatures.

As additional controls, two highly efficient enzyme-like catalysts and photocatalysts, Cu-N-C and CN_{mw}, were mixed into a nanocomposite (Cu-N-C/CN_{mw}, **Fig. S14** and **15**). As shown in **Fig. 3b**, Cu-N-C/CN_{mw} exhibited a gain effect under light irradiation; however, it reached only approximately one-third of that of $Cu_{SA}C_6N_6$. A series of characterizations, including electrochemical impedance spectra (EIS, **Fig. S16**), photoluminescence (PL) spectra (**Figs. S17**), and photoelectrochemical measurements (**Fig. S18**) of PCN, Cu-N-C/CN_{mw}, and $Cu_{SA}C_6N_6$ demonstrated a faster velocity of intramolecular charge migration in the C_6N_6 matrix than in PCN, and Cu-N-C/CN_{mw} played a crucial role in the boosted gain effect.

Considering that temperature induction is often used to obtain the gain effect, particularly in the photothermal manner in tumor therapies,[59] the influence of temperature on ABTS oxidation was also explored. As shown in **Fig. 3C and S19**, the peroxidase-like activity of $Cu_{SA}C_6N_6$ showed elevated velocity with the increase of temperature. When the temperature was increased from room temperature (25 °C) to 55 °C, the maximum limit for most lives that could endure, the catalytic activity reached 2 times of the original one, but was much smaller than that by mild light irradiation (3.6 times). In this sense, the gain reaction driven by the photocatalytic method was more efficient by a factor of 80% than that driven by the thermal stimuli.

The intrinsic mechanism of enhancement of the peroxidase-like activity of $Cu_{SA}C_6N_6$ under light irradiation was further investigated. In the first set of experiments, the temperature of the reactor after irradiation using the LED lamp was measured to exclude the photothermal effect. It was found that the irradiation for 10 min made the temperature only improve 3 ºC (**Fig. S20)**, whereas the practical reaction in this study only took 3 min, indicating an even smaller temperature fluctuation. The enhancement of peroxidase-like activity with such a minor increase in temperature was further measured (Fig. **S21** and **S22**), confirming that the photothermal-induced gain effect here was marginal. A series of control experiments, including examination of the oxidase-like activity of $Cu_{SA}C_6N_6$, direct photocatalytic oxidation of ABTS, and decomposition of H_2O_2, were also performed, which excluded the potential

interferences for the profound gain of peroxidase-like activity (**Fig. S23**). Moreover, the basic catalytic activity and photocatalytic processes of $Cu_{SA}C_6N_6$ can be easily modulated by tuning the Cu content and irradiation power density (**Fig. S24** and **S25**).

Coordinated basic and gain reactions mechanism of $Cu_{SA}C_6N_6$

To understand the coordinated basic and gain reaction mechanisms of $Cu_{SA}C_6N_6$ in peroxidase-like activity under light irradiation, the possible intermediate reactive species were first studied using scavenger trapping experiments. As illustrated in **Fig. S26**, both superoxide dismutase (SOD) and isopropanol, corresponding to the superoxide ($O_2^{\cdot-}$) and hydroxyl radical (·OH) scavengers, respectively, had negligible influence on the oxidation of ABTS catalyzed by $Cu_{SA}C_6N_6$, indicating that these two radicals were not formed during the activation of H_2O_2. Nevertheless, the catalytic activity was notably reduced when isopropanol was added to the reaction solution under light irradiation (**Fig. S27**), indicating that the redox reaction of H_2O_2 generated ·OH as a major step in $Cu_{SA}C_6N_6$ catalyzed ABTS oxidation. Other trapping experiments using radical probes such as nitrotetrazolium blue chloride (NBT) and coumarin (**Fig. S28** and **S29**), and electron spin resonance (ESR) spectra (**Fig. 4a, b**) also supported this speculation. For instance, there was no ESR signal for any ROS-trapping agent adduct, reminiscent of the case catalyzed by HRP. Interestingly, under light irradiation, a typical characteristic peak of the DMPO-·OH spin adduct with a typical signal intensity of 1:2:2:1 was observed (Fig. 4b), indicating the existence of ·OH, in agreement with the scavenger trapping experiments in **Fig. S27**.

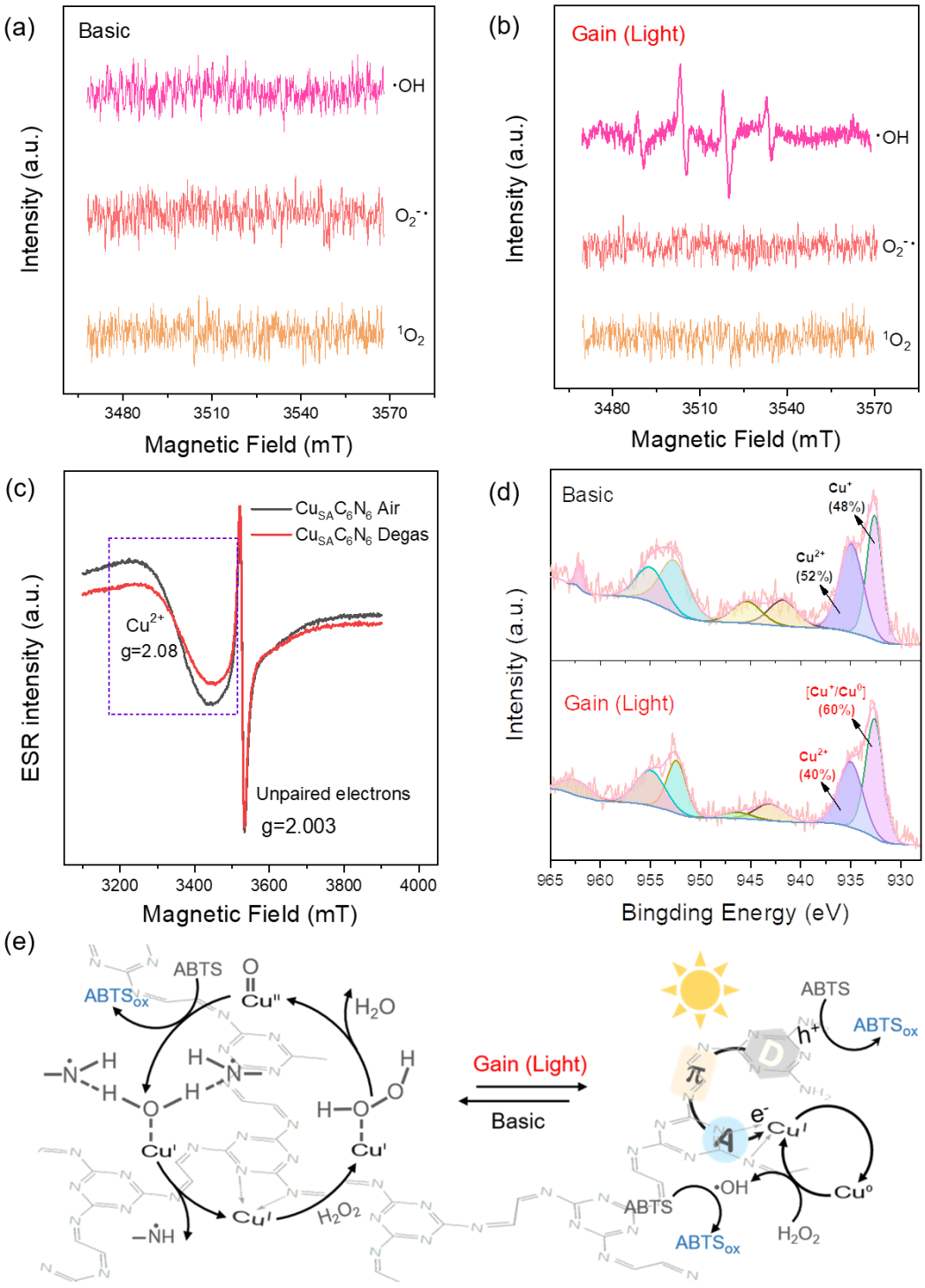

Fig. 4 Basic and gain reaction mechanisms for $Cu_SAC_6N_6$. ESR spectra of the spin adduct of ·OH, $O_2^{\cdot-}$, and $^1O_2$ generated during the activation of H_2O_2 by $Cu_SAC_6N_6$ in 0.2 M HAc-NaAc (pH 5.0) under the (a) basic and (b) gain reactions. (c) EPR spectra of $Cu_SAC_6N_6$ in air and after degassing at 200 °C in vacuum for 12 h. (d) XPS spectra of dynamic changes in the valence state of $Cu_SAC_6N_6$ in the light-on and light-off states. (e) Proposed mechanism for dual peroxidase-like and photocatalytic pathways mimicking the basic activity and gain effect using $Cu_SAC_6N_6$.

The solid-state ESR signal of $Cu_{SA}C_6N_6$ (**Fig. 4c**) further demonstrated the probability of the formation of Cu=O species during the peroxidase-like reaction. Given that Cu had a much stronger ESR intensity in air than in degassed conditions at g = 2.08, it was speculated that $Cu_{SA}C_6N_6$ might have a similar catalytic mechanism to HRP via a bound ROS pathway.[45] Meanwhile, to investigate the charge transfer as well as chemical-bond evolution of $Cu_{SA}C_6N_6$ under light irradiation, the synchronous illumination X-ray photoelectron spectroscopy (SI-XPS) technique was employed to clarify the dynamic changes of Cu-N.[60] As shown in **Fig. 4d**, the spectrum for Cu $2p^{3/2}$ was deconvoluted into two peaks at 932.6 and 934.8 eV, which were assigned to Cu^{1+} and Cu^{2+}, respectively. Interestingly, the percentage of Cu^{2+} decreased from 52% to 40% after light irradiation, while the percentage of Cu^{1+} and Cu^0 increased from 48% to 60%, supporting the acceptance of electrons for Cu atoms in the gain reaction.[61] Besides, as a significant amount of Cu^{2+} was retained under light irradiation, the basic reaction pathway should also be activated during the gain reaction that was much more efficient.

Taking all these experimental evidences into consideration, the mechanism for the light-gained peroxidase-like catalytic activity of $Cu_{SA}C_6N_6$ was proposed (**Fig. 4e**). Briefly, in the basic reaction, H_2O_2 was first bound to the N-coordinated metal site of Cu^I in $Cu_{SA}C_6N_6$ to form Cu^I-superoxo species. Then, O-O cleavage occurred to decompose the adsorbed H_2O_2 into H_2O upon the oxidation of Cu^I to Cu^{II}=O. Next, the Cu^{II}=O was reduced by the ABTS substrate owing to the affinity of ABTS for Cu^{II}=O and the electron-donating ability of ABTS. In contrast, when the light was turned on, the photocatalytic processes were activated, providing a new pathway for enhancing the catalytic activity. The terminal mixed-valence Cu species emerged as collectors of photogenerated electrons, and these photoelectrons subsequently reduced Cu^+ to Cu^0. Subsequently, Cu^0 contributed to the in situ decomposition of H_2O_2 to produce ·OH via a Fenton-like process.[62] Finally, H_2O_2 oxidized Cu^0 to promote the formation of Cu^+ species, completing the photocatalytic cycle and maintaining the mixed valence states.

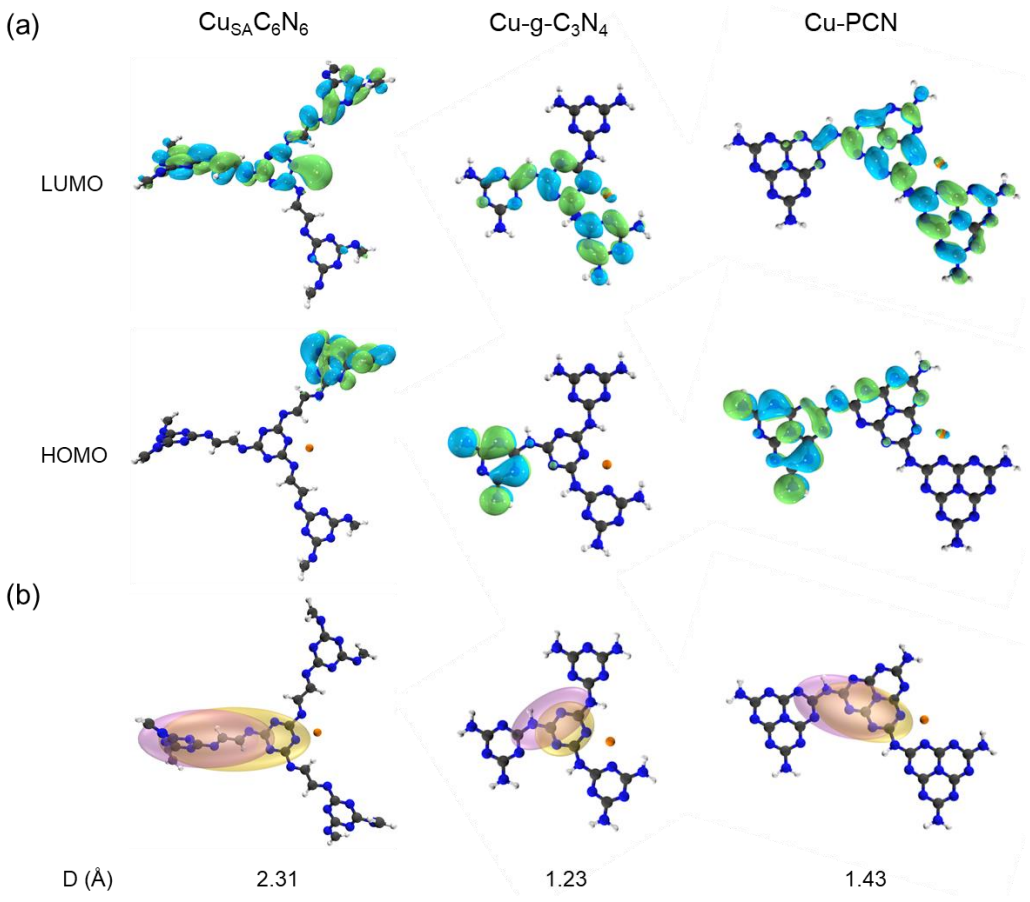

Fig. 5 (a) DFT computed the molecular frontier orbital isosurfaces of the LUMO and HOMO for $Cu_{SA}C_6N_6$, Cu-g-C_3N_4, and Cu-PCN. (b) Calculated smooth description of electron (yellow isosurface) and hole (pink isosurface) spatial population distributions in $Cu_{SA}C_6N_6$, Cu-g-C_3N_4, and Cu-PCN. Carbon atoms (black), Nitrogen atoms (blue), Hydrogen atoms (white), Cu atoms (orange).

The aforementioned results further demonstrated that $Cu_{SA}C_6N_6$ not only had a peroxidase-like Cu-N coordination active center but also owned an unusual donor-π-acceptor (D-π-A) unit (**Fig. 1h**),[62-64] where the single Cu atom acted as an electron acceptor, the triazine rings emerged as electron donors (photovoltaic center), and the -N=CH-CH=N- linkers offered π-conjugated charge transfer channels for D-A couples. These π-interconnected D-A couples played a crucial role in addressing the inconsistency of requirements for basic and gain reactions by not only reducing recombination (control sample: Cu^{2+}-PCN) and promoting charge separation (control sample: Cu-N-C), but also accelerating intramolecular charge transfer (control sample: Cu-N-C/CN_{mw}). These results were further supported by DFT calculations of electron

density and centroid distance (**Fig. 5**). As controls, the Cu-g-C_3N_4 (where the N atom substituted the -N=CH-CH=N- linkers) and Cu-PCN were computed (**Fig. S30** and **Table S3**). It was observed that in the HOMO state (**Fig. 5a**), the electron density mainly resided on the triazine/heptazine ring units in the molecular fragments of $Cu_SAC_6N_6$, Cu-g-C_3N_4 and Cu-PCN. Interestingly, for the LUMO state, electrons delocalized on $Cu_SAC_6N_6$ were transferred from three equivalent triazine ring units to both -N=CH-CH=N- linkers and Cu atoms (**Fig. S31**), whereas electrons in Cu-g-C_3N_4 and Cu-PCN transitioned to other triazine/heptazine ring units, resulting in few electrons delocalized on the Cu atom moieties (**Fig. S32-S33**). Thus, owing to the π-conjugated linkers, $Cu_SAC_6N_6$ underwent more intramolecular charge transfer from the triazine ring unit to the Cu atom than Cu-g-C_3N_4 and Cu-PCN upon light irradiation.

Moreover, the electron/hole population during excitation and the absorption spectra of the repeat units of $Cu_SAC_6N_6$, Cu-g-C_3N_4, and Cu-PCN also demonstrate the crucial role of π-interconnected D-A couples (**Fig. 5b** and **Fig. S34**). For Cu-g-C_3N_4, the triazine ring unit directly bound to Cu endowed the centroid distance of electrons and holes at 1.23 Å. This value was close to that of Cu-PCN (1.43), where the Cu atoms were anchored on the heptazine cavity skeleton, leading to rapid electron-hole recombination without outside assistance. Interestingly, after inserting the -N=CH-CH=N- linkers in $Cu_SAC_6N_6$, the attraction of metal atoms and electrons was reinforced, further increasing the centroid distance of the electrons and holes to 2.31 Å. Such conspicuous spatial separation would not only reduce the recombination of electrons and holes, but also promote intramolecular charge separation and migration, which well addressed inconsistency of requirements for basic and gain reactions.

Adaptable sensing of Glucose

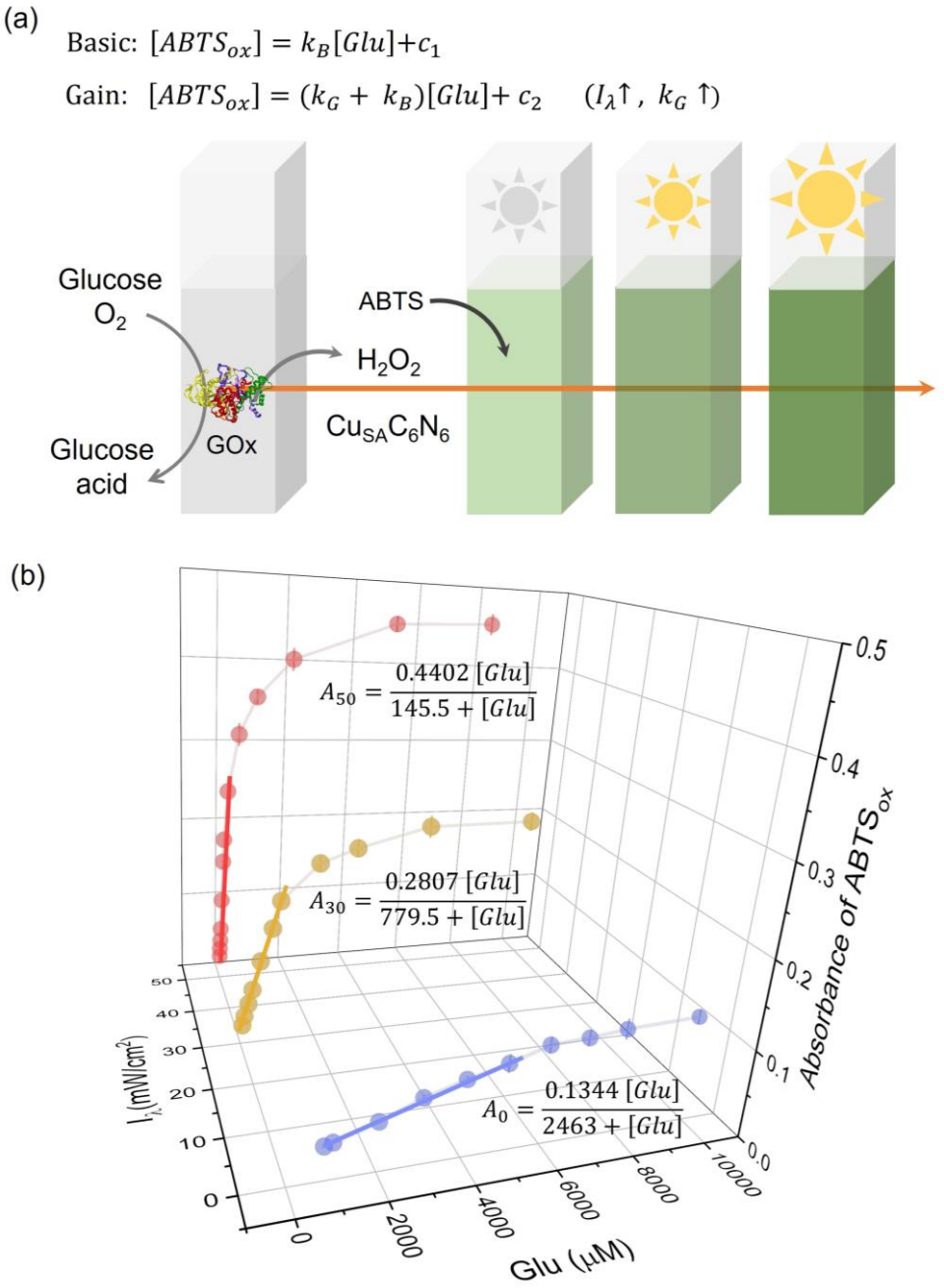

Fig. 6 (a) Principle of adaptable sensing of glucose based on $Cu_{SA}C_6N_6$. Inset: rate equations of basic and gain reactions under tuned light intensity (I_λ). k_B and k_G are the intrinsic rate constants of the basic and gain reactions, respectively. c_1 and c_2 are constants. (b) Absorbance of $ABTS_{ox}$ at 417 nm catalyzed by $Cu_{SA}C_6N_6$ with different concentrations of glucose in the presence of glucose oxidase under tuned light intensity. Inset: non-linear rate equations of basic and gain reactions with different concentrations of glucose. Bold lines are linear relationship between the absorbance of $ABTS_{ox}$ at 417 nm and concentrations of glucose under tuned light intensity.

Improving quality of life is an enduring topic in modern society. Therefore, the intelligent response of glucose has received increasing attention as a powerful tool in the field of human health. In recent years, many biosensing methods for detecting glucose based on nanozymes have found broad utility owing to their simplicity, sensitivity, and high selectivity.[65-67] Despite enormous advances, in vitro recording of the narrow linear concentration range of glucose cannot directly provide physiological information for better comprehension of the dynamic fluctuation of glucose in the brain.[69] Intelligent response to glucose with a random concentration range at a single sensing interface in vivo is highly envisioned to understand the pathological process, but still faces great challenges.

As a proof of this concept, we propose an intelligent response sensor for monitoring glucose in vitro (**Fig. 6a**). As shown in **Fig. 6b**, for the conventional biosensors (0 W/cm^2), at a low concentration range, the absorbance of $ABTS_{ox}$ at 417 nm was proportional to the first order with glucose. In the high concentration range, the absorbance reached a plateau, leading to a limited detection range. In this sense, relating the response with full-scale analyte concentrations at logarithmic scale primarily considering a fitting coefficient of determination (R^2) close to 1 is widely used, but is questioned in uncertainty in theory.[70] In principle, a reliable fitting should follow the signal transformation mechanism rather than merely the data statistics.[71] Nonetheless, although the strict non-linear rate equations (**Fig. 6b, inset**) could match the experimental data well (see the fitted calibration curve in **Fig. 6b**), it was noted that at the plateau region, the slopes were essentially zero, indicating an extremely poor sensitivity.

Developing adaptive sensitivity and linear detection concentration ranges is an ideal solution to obtain a strict full-scale range of reliable detection. As shown in **Fig. 6b,** glucose was normally detected in a linear range of 800 - 6000 μM. The linear range can be extended from 50 - 1000 μM at 30 mW/cm^2 to 5 - 80 μM at 50 mW/cm^2. At the same manner, the limit of detection (LOD) for glucose was tuned from 195.02 μM in the normal mode, to 15.07 μM and 1.20 μM under irradiation at 30 and 50 mW/cm^2,

respectively. The rate equations in **Fig. 6a inset** (see the detailed elementary reactions and derivations in **SI**) well supported these facts that the concentration of $ABTS_{ox}$ was in linear with that of glucose, and the slope (i.e., sensing sensitivity) was positively correlated with light intensity. Therefore, a full-scale range of reliable detection could be successfully realized by intelligent switching among different ranges of a single sensor in the measuring progress, enabled by high adaptability of $Cu_{SA}C_6N_6$ using basic and gain reactions.

Due to limited room, intelligent artificial devices are preferred to equip biosensors as few as possible and mechanically switching of them would lead to a low operation efficiency. In this sense, one single biosensor with adaptable linear detection range and sensitivity via automatic light switch would be helpful. It is foreseeable that further considering the intrinsic outstanding temporal and spatial resolution of light irradiation, this intelligent biosensor would supply a prospective candidate for dynamic chemical noses for intelligent artificial devices, such as robots, brain-machine interface, and internet-to-things in a high level of integration.

Conclusion

In summary, we proposed a Cu single atom catalyst on a highly conjugated carbon nitride ($Cu_{SA}C_6N_6$) to address the inconsistency of requirements for basic and gain reactions in mimicking self-adaptability from nature. $Cu_{SA}C_6N_6$ had single Cu atoms, repetitive triazine cores, and -N=CH-CH=N- linkers, which successfully coordinated the peroxidase-like Cu-N coordination center and the light responsive donor-π-acceptor (D-π-A) unit with promoted intramolecular charge separation and migration. Accordingly, $Cu_{SA}C_6N_6$ could not only drive the basic ABTS oxidation through bound high-valent copper-oxo pathway, but also undertake a second gain reaction triggered by light via free hydroxyl radical pathway under the same conditions. As a result of crucial multiformity of reactive oxygen-related intermediates in the same oxidation reaction, $Cu_{SA}C_6N_6$ demonstrated conspicuous basic catalytic oxidation activity and a superb

gain up to 3.6 times under household light. This performance was significantly higher than that of the control systems, including solo carbon nitride-based nanozyme or photocatalyst, their mixtures, and even that under thermal stimuli (by a factor of 80% rising from room temperature to 55 ^{o}C, the maximum temperature for most lives that can endure). As a proof-of-concept application, $Cu_{SA}C_6N_6$ was successfully applied in a biosensor of glucose, which intelligently switched linear detection range and sensitivity to a diverse range of concentrations in vitro, simply by tuning the light intensity. It is high envisioned that self-adaptive $Cu_{SA}C_6N_6$ along with the further intrinsic temporal and spatial resolution of light, would supply a prospective candidate for adaptable chemical noses for artificial devices, such as robots, brain-machine interface, and internet-to-things in a higher level of integration.

Acknowledgements

This work was supported by the National Natural Science Foundation of China (22174014, 22074015), and the Fundamental Research Funds for the Central Universities. We thank Prof. Yingpu Bi (Lanzhou Institute of Chemical Physics) for offering synchronous illumination X-ray photoelectron spectroscopy (SI-XPS) technique.

Conflict of interest

The authors declare no conflict of interest.

References

1. Wang, X. Q.; Chan, K. H.; Cheng, Y.; Ding, T.; Li, T.; Achavananthadith, S.; Ahmet, S.; Ho, J. S.; Ho, G. W., Somatosensory, Light-Driven, Thin-Film Robots Capable of Integrated Perception and Motility. *Adv. Mater.* **2020,** *32*, 2000351-2000360.
2. Liao, F.; Zhou, Z.; Kim, B. J.; Chen, J.; Wang, J.; Wan, T.; Zhou, Y.; Hoang, A. T.; Wang, C.; Kang, J.; Ahn, J.-H.; Chai, Y., Bioinspired in-sensor visual adaptation for

accurate perception. *Nat. Electron.* **2022,** *5*, 84-91.

3. Potyrailo, R. A., Multivariable Sensors for Ubiquitous Monitoring of Gases in the Era of Internet of Things and Industrial Internet. *Chem. Rev.* **2016,** *116*, 11877-11923.

4. Zhang, X.; Xie, X.; Wang, H.; Zhang, J.; Pan, B.; Xie, Y., Enhanced Photoresponsive Ultrathin Graphitic-Phase C_3N_4 Nanosheets for Bioimaging. *J. Am. Chem. Soc.* **2012,** *135*, 18-21.

5. Wang, F.; Zhang, Y.; Du, Z.; Ren, J.; Qu, X., Designed heterogeneous palladium catalysts for reversible light-controlled bioorthogonal catalysis in living cells. *Nat. Commun.* **2018,** *9*, 1209-1217.

6. Neri, S.; Garcia Martin, S.; Pezzato, C.; Prins, L. J., Photoswitchable Catalysis by a Nanozyme Mediated by a Light-Sensitive Cofactor. *J. Am. Chem. Soc.* **2017,** *139*, 1794-1797.

7. Zhang, J.; Wu, S.; Lu, X.; Wu, P.; Liu, J., Lanthanide-Boosted Singlet Oxygen from Diverse Photosensitizers along with Potent Photocatalytic Oxidation. *ACS Nano* **2019,** *13*, 14152-14161.

8. Liu, Y.; Wang, X.; Wang, Q.; Zhang, Y.; Liu, Q.; Liu, S.; Li, S.; Du, Y.; Wei, H., Structurally Engineered Light-Responsive Nanozymes for Enhanced Substrate Specificity. *Anal. Chem.* **2021,** *93*, 15150-15158.

9. Li, S.; Shang, L.; Xu, B.; Wang, S.; Gu, K.; Wu, Q.; Sun, Y.; Zhang, Q.; Yang, H.; Zhang, F.; Gu, L.; Zhang, T.; Liu, H., A Nanozyme with Photo-Enhanced Dual Enzyme-Like Activities for Deep Pancreatic Cancer Therapy. *Angew. Chem. Int. Ed.* **2019,** *58*, 12624-12631.

10. Rudroff, F.; Mihovilovic, M. D.; Gröger, H.; Snajdrova, R.; Iding, H.; Bornscheuer, U. T., Opportunities and challenges for combining chemo- and biocatalysis. *Nat. Catal.* **2018,** *1*, 12-22.

11. Wang, X.; Maeda, K.; Thomas, A.; Takanabe, K.; Xin, G.; Carlsson, J. M.; Domen, K.; Antonietti, M., A metal-free polymeric photocatalyst for hydrogen production from water under visible light. *Nat. Mater.* **2008,** *8*, 76-80.

12. Ghosh, I.; Khamrai, J.; Savateev, A.; Shlapakov, N.; Antonietti, M.; König, B.,

Organic semiconductor photocatalyst can bifunctionalize arenes and heteroarenes. *Science* **2019,** *365*, 360-366.

13. Zhao, D.; Wang, Y.; Dong, C.-L.; Huang, Y.-C.; Chen, J.; Xue, F.; Shen, S.; Guo, L., Boron-doped nitrogen-deficient carbon nitride-based Z-scheme heterostructures for photocatalytic overall water splitting. *Nat. Energy* **2021,** *6*, 388-397.

14. Teng, Z.; Zhang, Q.; Yang, H.; Kato, K.; Yang, W.; Lu, Y.-R.; Liu, S.; Wang, C.; Yamakata, A.; Su, C.; Liu, B.; Ohno, T., Atomically dispersed antimony on carbon nitride for the artificial photosynthesis of hydrogen peroxide. *Nat. Catal.* **2021,** *4*, 374-384.

15. Volokh, M.; Peng, G.; Barrio, J.; Shalom, M., Carbon Nitride Materials for Water Splitting Photoelectrochemical Cells. *Angew. Chem. Int. Ed.* **2019,** *58*, 6138-6151.

16. Kuriki, R.; Sekizawa, K.; Ishitani, O.; Maeda, K., Visible-Light-Driven CO_2 Reduction with Carbon Nitride: Enhancing the Activity of Ruthenium Catalysts. *Angew. Chem. Int. Ed.* **2015,** *54*, 2406-2409.

17. Ong, W.-J.; Tan, L.-L.; Ng, Y. H.; Yong, S.-T.; Chai, S.-P., Graphitic Carbon Nitride (g-C_3N_4)-Based Photocatalysts for Artificial Photosynthesis and Environmental Remediation: Are We a Step Closer To Achieving Sustainability? *Chem. Rev.* **2016,** *116*, 7159-7329.

18. Lakhi, K. S.; Park, D.-H.; Al-Bahily, K.; Cha, W.; Viswanathan, B.; Choy, J.-H.; Vinu, A., Mesoporous carbon nitrides: synthesis, functionalization, and applications. *Chem. Soc. Rev.* **2017,** *46*, 72-101.

19. Schlomberg, H.; Kröger, J.; Savasci, G.; Terban, M. W.; Bette, S.; Moudrakovski, I.; Duppel, V.; Podjaski, F.; Siegel, R.; Senker, J.; Dinnebier, R. E.; Ochsenfeld, C.; Lotsch, B. V., Structural Insights into Poly (Heptazine Imides): A Light-Storing Carbon Nitride Material for Dark Photocatalysis. *Chem. Mater.* **2019,** *31*, 7478-7486.

20. Liu, M.; Wei, C.; Zhuzhang, H.; Zhou, J.; Pan, Z.; Lin, W.; Yu, Z.; Zhang, G.;

Wang, X., Fully Condensed Poly (Triazine Imide) Crystals: Extended π-Conjugation and Structural Defects for Overall Water Splitting. *Angew. Chem. Int. Ed.* **2021,** *61*, 202113389-202113394.

21. Wu, W.; Huang, L.; Wang, E.; Dong, S., Atomic engineering of single-atom nanozymes for enzyme-like catalysis. *Chem. Sci.* **2020,** *11*, 9741-9756.

22. Chen, Z.; Mitchell, S.; Vorobyeva, E.; Leary, R. K.; Hauert, R.; Furnival, T.; Ramasse, Q. M.; Thomas, J. M.; Midgley, P. A.; Dontsova, D.; Antonietti, M.; Pogodin, S.; López, N.; Pérez-Ramírez, J., Stabilization of Single Metal Atoms on Graphitic Carbon Nitride. *Adv. Funct. Mater.* **2017,** *27*, 1605785.

23. Wang, Y.; Mao, J.; Meng, X.; Yu, L.; Deng, D.; Bao, X., Catalysis with Two-Dimensional Materials Confining Single Atoms: Concept, Design, and Applications. *Chem. Rev.* **2018,** *119*, 1806-1854.

24. Yang, H.; Zhou, Q.; Fang, Z.; Li, W.; Zheng, Y.; Ma, J.; Wang, Z.; Zhao, L.; Liu, S.; Shen, Y.; Zhang, Y., Carbon nitride of five-membered rings with low optical bandgap for photoelectrochemical biosensing. *Chem* **2021,** *7*, 2708-2721.

25. Ma, J.; Peng, X.; Zhou, Z.; Yang, H.; Wu, K.; Fang, Z.; Han, D.; Fang, Y.; Liu, S.; Shen, Y.; Zhang, Y., Extended Conjugation Tuning Carbon Nitride for Non-sacrificial H_2O_2 Photosynthesis and Hypoxic Tumor Therapy. *Angew. Chem. Int. Ed.* **2022,** *61*, 202210856-202210865.

26. Mahmood, J.; Lee, E. K.; Jung, M.; Shin, D.; Jeon, I.-Y.; Jung, S.-M.; Choi, H.-J.; Seo, J.-M.; Bae, S.-Y.; Sohn, S.-D.; Park, N.; Oh, J. H.; Shin, H.-J.; Baek, J.-B., Nitrogenated holey two-dimensional structures. *Nat. Commun.* **2015,** *6*, 6486-6493.

27. Zhou, G.; Shan, Y.; Hu, Y.; Xu, X.; Long, L.; Zhang, J.; Dai, J.; Guo, J.; Shen, J.; Li, S.; Liu, L.; Wu, X., Half-metallic carbon nitride nanosheets with micro grid mode resonance structure for efficient photocatalytic hydrogen evolution. *Nat. Commun.* **2018,** *9*, 3366-3375.

28. Kumar, P.; Vahidzadeh, E.; Thakur, U. K.; Kar, P.; Alam, K. M.; Goswami, A.; Mahdi, N.; Cui, K.; Bernard, G. M.; Michaelis, V. K.; Shankar, K., C_3N_5: A Low Bandgap Semiconductor Containing an Azo-Linked Carbon Nitride Framework for

Photocatalytic, Photovoltaic and Adsorbent Applications. *J. Am. Chem. Soc.* **2019,** *141*, 5415-5436.

29. Kim, I. Y.; Kim, S.; Jin, X.; Premkumar, S.; Chandra, G.; Lee, N. S.; Mane, G. P.; Hwang, S. J.; Umapathy, S.; Vinu, A., Ordered Mesoporous C_3N_5 with a Combined Triazole and Triazine Framework and Its Graphene Hybrids for the Oxygen Reduction Reaction (ORR). *Angew. Chem. Int. Ed.* **2018,** *57*, 17135-17140.

30. Mahmood, J.; Lee, E. K.; Jung, M.; Shin, D.; Choi, H.-J.; Seo, J.-M.; Jung, S.-M.; Kim, D.; Li, F.; Lah, M. S.; Park, N.; Shin, H.-J.; Oh, J. H.; Baek, J.-B., Two-dimensional polyaniline (C_3N) from carbonized organic single crystals in solid state. *P. Acad. Nat. Sci.* **2016,** *113*, 7414-7419.

31. Han, D.; Yang, H.; Zhou, Z.; Wu, K.; Ma, J.; Fang, Y.; Hong, Q.; Xi, G.; Liu, S.; Shen, Y.; Zhang, Y., Photoelectron Storages in Functionalized Carbon Nitrides for Colorimetric Sensing of Oxygen. *ACS Sens.* **2022,** *7*, 2328-2337.

32. Zhang, T.; Zhang, D.; Han, X.; Dong, T.; Guo, X.; Song, C.; Si, R.; Liu, W.; Liu, Y.; Zhao, Z., Preassembly Strategy To Fabricate Porous Hollow Carbonitride Spheres Inlaid with Single Cu–N_3 Sites for Selective Oxidation of Benzene to Phenol. *J. Am. Chem. Soc.* **2018,** *140*, 16936-16940.

33. Wang, W.; Deng, C.; Xie, S.; Li, Y.; Zhang, W.; Sheng, H.; Chen, C.; Zhao, J., Photocatalytic C–C Coupling from Carbon Dioxide Reduction on Copper Oxide with Mixed-Valence Copper(I)/Copper(II). *J. Am. Chem. Soc.* **2021,** *143*, 2984-2993.

34. Cai, J.; Huang, J.; Wang, S.; Iocozzia, J.; Sun, Z.; Sun, J.; Yang, Y.; Lai, Y.; Lin, Z., Crafting Mussel-Inspired Metal Nanoparticle-Decorated Ultrathin Graphitic Carbon Nitride for the Degradation of Chemical Pollutants and Production of Chemical Resources. *Adv. Mater.* **2019,** *31*, 1806314-1806325.

35. Liang, Y.; Xu, W.; Fang, J.; Liu, Z.; Chen, D.; Pan, T.; Yu, Y.; Fang, Z., Highly dispersed bismuth oxide quantum dots/graphite carbon nitride nanosheets heterojunctions for visible light photocatalytic redox degradation of environmental pollutants. *Appl. Catal. B-environ* **2021,** *295*, 120279-120291.

36. Huang, C.; Wen, Y.; Ma, J.; Dong, D.; Shen, Y.; Liu, S.; Ma, H.; Zhang, Y.,

Unraveling fundamental active units in carbon nitride for photocatalytic oxidation reactions. *Nat. Commun.* **2021,** *12*, 320-328.

37. Teng, Z.; Yang, N.; Lv, H.; Wang, S.; Hu, M.; Wang, C.; Wang, D.; Wang, G., Edge-Functionalized g-C_3N_4 Nanosheets as a Highly Efficient Metal-free Photocatalyst for Safe Drinking Water. *Chem* **2019,** *5*, 664-680.

38. Fan, K.; Xi, J.; Fan, L.; Wang, P.; Zhu, C.; Tang, Y.; Xu, X.; Liang, M.; Jiang, B.; Yan, X.; Gao, L., In vivo guiding nitrogen-doped carbon nanozyme for tumor catalytic therapy. *Nat. Commun.* **2018,** *9*, 1440 -1451.

39. Zhou, Q.; Yang, H.; Chen, X.; Xu, Y.; Han, D.; Zhou, S.; Liu, S.; Shen, Y.; Zhang, Y., Cascaded Nanozyme System with High Reaction Selectivity by Substrate Screening and Channeling in a Microfluidic Device. *Angew. Chem. Int. Ed.* **2021,** *61*, 202112453-202112459.

40. Zhang, P.; Sun, D.; Cho, A.; Weon, S.; Lee, S.; Lee, J.; Han, J. W.; Kim, D.-P.; Choi, W., Modified carbon nitride nanozyme as bifunctional glucose oxidase-peroxidase for metal-free bioinspired cascade photocatalysis. *Nat. Commun.* **2019,** *10*, 940-954.

41. Huang, Y.; Ren, J.; Qu, X., Nanozymes: Classification, Catalytic Mechanisms, Activity Regulation, and Applications. *Chem. Rev.* **2019,** *119*, 4357-4412.

42. Vázquez-González, M.; Liao, W.-C.; Cazelles, R.; Wang, S.; Yu, X.; Gutkin, V.; Willner, I., Mimicking Horseradish Peroxidase Functions Using Cu^{2+}-Modified Carbon Nitride Nanoparticles or Cu^{2+}-Modified Carbon Dots as Heterogeneous Catalysts. *ACS Nano* **2017,** *11*, 3247-3253.

43. Ju, E.; Dong, K.; Chen, Z.; Liu, Z.; Liu, C.; Huang, Y.; Wang, Z.; Pu, F.; Ren, J.; Qu, X., Copper(II)-Graphitic Carbon Nitride Triggered Synergy: Improved ROS Generation and Reduced Glutathione Levels for Enhanced Photodynamic Therapy. *Angew. Chem. Int. Ed.* **2016,** *55*, 11467-11471.

44. Wu, J.; Wang, X.; Wang, Q.; Lou, Z.; Li, S.; Zhu, Y.; Qin, L.; Wei, H., Nanomaterials with enzyme-like characteristics (nanozymes): next-generation artificial enzymes (II). *Chem. Soc. Rev.* **2019,** *48*, 1004-1076.

45. Chen, X.; Zhao, L.; Wu, K.; Yang, H.; Zhou, Q.; Xu, Y.; Zheng, Y.; Shen, Y.; Liu, S.; Zhang, Y., Bound oxygen-atom transfer endows peroxidase-mimic M–N–C with high substrate selectivity. *Chem. Sci.* **2021,** *12*, 8865-8871.

46. Ji, S.; Jiang, B.; Hao, H.; Chen, Y.; Dong, J.; Mao, Y.; Zhang, Z.; Gao, R.; Chen, W.; Zhang, R.; Liang, Q.; Li, H.; Liu, S.; Wang, Y.; Zhang, Q.; Gu, L.; Duan, D.; Liang, M.; Wang, D.; Yan, X.; Li, Y., Matching the kinetics of natural enzymes with a single-atom iron nanozyme. *Nat. Catal.* **2021,** *4*, 407-417.

47. Zhang, R.; Xue, B.; Tao, Y.; Zhao, H.; Zhang, Z.; Wang, X.; Zhou, X.; Jiang, B.; Yang, Z.; Yan, X.; Fan, K., Edge-Site Engineering of Defective Fe–N_4 Nanozymes with Boosted Catalase-Like Performance for Retinal Vasculopathies. *Adv. Mater.* **2022,** *34*, 202205324-202205337.

48. Jiao, L.; Wu, J.; Zhong, H.; Zhang, Y.; Xu, W.; Wu, Y.; Chen, Y.; Yan, H.; Zhang, Q.; Gu, W.; Gu, L.; Beckman, S. P.; Huang, L.; Zhu, C., Densely Isolated FeN_4 Sites for Peroxidase Mimicking. *ACS Catal.* **2020,** *10*, 6422-6429.

49. Wan, K.; Jiang, B.; Tan, T.; Wang, H.; Liang, M., Surface-Mediated Production of Complexed •OH Radicals and Fe=O Species as a Mechanism for Iron Oxide Peroxidase-Like Nanozymes. *Small* **2022**, 2204372-2204379.

50. Chang, M.; Hou, Z.; Wang, M.; Yang, C.; Wang, R.; Li, F.; Liu, D.; Peng, T.; Li, C.; Lin, J., Single-Atom Pd Nanozyme for Ferroptosis-Boosted Mild-Temperature Photothermal Therapy. *Angew. Chem. Int. Ed.* **2021,** *60*, 12971-12979.

51. Wang, H.; Jiang, D.; Huang, D.; Zeng, G.; Xu, P.; Lai, C.; Chen, M.; Cheng, M.; Zhang, C.; Wang, Z., Covalent triazine frameworks for carbon dioxide capture. *J. Mater. Chem. A* **2019,** *7*, 22848-22870.

52. Devautour-Vinot, S.; Maurin, G.; Serre, C.; Horcajada, P.; Paula da Cunha, D.; Guillerm, V.; de Souza Costa, E.; Taulelle, F.; Martineau, C., Structure and Dynamics of the Functionalized MOF Type UiO-66(Zr): NMR and Dielectric Relaxation Spectroscopies Coupled with DFT Calculations. *Chem. Mater.* **2012,** *24*, 2168-2177.

53. Zhu, X.; Tian, C.; Mahurin, S. M.; Chai, S.-H.; Wang, C.; Brown, S.; Veith, G. M.; Luo, H.; Liu, H.; Dai, S., A Superacid-Catalyzed Synthesis of Porous Membranes

Based on Triazine Frameworks for CO_2 Separation. *J. Am. Chem. Soc.* **2012,** *134*, 10478-10484.

54. Xiao, X.; Gao, Y.; Zhang, L.; Zhang, J.; Zhang, Q.; Li, Q.; Bao, H.; Zhou, J.; Miao, S.; Chen, N.; Wang, J.; Jiang, B.; Tian, C.; Fu, H., A Promoted Charge Separation/Transfer System from Cu Single Atoms and C_3N_4 Layers for Efficient Photocatalysis. *Adv. Mater.* **2020,** *32*, 2003082-2003090.

55. Liu, H.; Li, X.; Ma, Z.; Sun, M.; Li, M.; Zhang, Z.; Zhang, L.; Tang, Z.; Yao, Y.; Huang, B.; Guo, S., Atomically Dispersed Cu Catalyst for Efficient Chemoselective Hydrogenation Reaction. *Nano Lett.* **2021,** *21*, 10284-10291.

56. Sun, T.; Li, Y.; Cui, T.; Xu, L.; Wang, Y.-G.; Chen, W.; Zhang, P.; Zheng, T.; Fu, X.; Zhang, S.; Zhang, Z.; Wang, D.; Li, Y., Engineering of Coordination Environment and Multiscale Structure in Single-Site Copper Catalyst for Superior Electrocatalytic Oxygen Reduction. *Nano Lett.* **2020,** *20*, 6206-6214.

57. Yang, J.; Liu, W.; Xu, M.; Liu, X.; Qi, H.; Zhang, L.; Yang, X.; Niu, S.; Zhou, D.; Liu, Y.; Su, Y.; Li, J.-F.; Tian, Z.-Q.; Zhou, W.; Wang, A.; Zhang, T., Dynamic Behavior of Single-Atom Catalysts in Electrocatalysis: Identification of Cu-N_3 as an Active Site for the Oxygen Reduction Reaction. *J. Am. Chem. Soc.* **2021,** *143*, 14530-14539.

58. Rahim, M. A.; Tang, J.; Christofferson, A. J.; Kumar, P. V.; Meftahi, N.; Centurion, F.; Cao, Z.; Tang, J.; Baharfar, M.; Mayyas, M.; Allioux, F.-M.; Koshy, P.; Daeneke, T.; McConville, C. F.; Kaner, R. B.; Russo, S. P.; Kalantar-Zadeh, K., Low-temperature liquid platinum catalyst. *Nat. Chem.* **2022,** *14*, 935-941.

59. Zhang, L.; Long, R.; Zhang, Y.; Duan, D.; Xiong, Y.; Zhang, Y.; Bi, Y., Direct Observation of Dynamic Bond Evolution in Single-Atom Pt/C_3N_4 Catalysts. *Angew. Chem. Int. Ed.* **2020,** *59*, 6224-6229.

60. Luo, L.; Gong, Z.; Xu, Y.; Ma, J.; Liu, H.; Xing, J.; Tang, J., Binary Au-Cu Reaction Sites Decorated ZnO for Selective Methane Oxidation to C1 Oxygenates with Nearly 100% Selectivity at Room Temperature. *J. Am. Chem. Soc.* **2021,** *144*, 740-750.

61. Zhou, Y.; Zhang, L.; Wang, W., Direct functionalization of methane into

ethanol over copper modified polymeric carbon nitride via photocatalysis. *Nat. Commun.* **2019,** *10*, 506-514.

62. Shiraishi, Y.; Takii, T.; Hagi, T.; Mori, S.; Kofuji, Y.; Kitagawa, Y.; Tanaka, S.; Ichikawa, S.; Hirai, T., Resorcinol–formaldehyde resins as metal-free semiconductor photocatalysts for solar-to-hydrogen peroxide energy conversion. *Nat. Mater.* **2019,** *18*, 985-993.

63. Zhang, L.; Morshedi, M.; Kodikara, M. S.; Humphrey, M. G., Giant Multi-Photon Absorption by Heptazine Organometalation. *Angew. Chem. Int. Ed.* **2022,** *61*, 202208168-202208173.

64. Fan, X.; Zhang, L.; Cheng, R.; Wang, M.; Li, M.; Zhou, Y.; Shi, J., Construction of Graphitic C_3N_4-Based Intramolecular Donor–Acceptor Conjugated Copolymers for Photocatalytic Hydrogen Evolution. *ACS Catal.* **2015,** *5*, 5008-5015.

65. Wei, H.; Wang, E., Fe_3O_4 Magnetic Nanoparticles as Peroxidase Mimetics and Their Applications in H_2O_2 and Glucose Detection. *Anal. Chem.* **2008,** *80*, 2250-2254.

66. Wang, L.; Shao, H.; Lu, X.; Wang, W.; Zhang, J.-R.; Song, R.-B.; Zhu, J.-J., A glucose/O_2 fuel cell-based self-powered biosensor for probing a drug delivery model with self-diagnosis and self-evaluation. *Chem. Sci.* **2018,** *9*, 8482-8491.

67. Wang, Q.; Zhang, X.; Huang, L.; Zhang, Z.; Dong, S., GOx@ZIF-8(NiPd) Nanoflower: An Artificial Enzyme System for Tandem Catalysis. *Angew. Chem. Int. Ed.* **2017,** *56*, 16082-16085.

68. Ye, X.; Wang, X.; Kong, Y.; Dai, M.; Han, D.; Liu, Z., FRET Modulated Signaling: A Versatile Strategy to Construct Photoelectrochemical Microsensors for In Vivo Analysis. *Angew. Chem. Int. Ed.* **2021,** *133*, 11880-11884.

69. Urban, P. L., Please Avoid Plotting Analytical Response against Logarithm of Concentration. *Anal. Chem.* **2020,** *92*, 10210-10212.

70. Hong, Q.; Shen, Y.; Liu, S.; Zhang, Y., Re-Examination of Plotting Analytical Response against Different Forms of Concentration. *Anal. Chem.* **2021,** *93*, 11910-11914.